Supporting Information for

Zeolite-Supported Bimetallic Catalyst: Controlling Selectivity of Rhodium Complexes by Nearby Iridium Complexes

Jing Lu, Claudia Martinez-Macias, Ceren Aydin, Nigel D. Browning, Bruce C. Gates*

Materials and Sample Preparation. Standard methods were used for sample synthesis and handling with the exclusion of moisture and air. H_2 was supplied by Airgas (99.999%) and purified by passage through traps containing reduced Cu/Al_2O_3 and activated zeolite 4A to remove traces of O_2 and moisture, respectively. Helium (Airgas, 99.999%) and ethylene (Airgas, 99.99%) were purified by passage through similar traps. CO (Matheson, 99.999%), in a 10% mixture in helium, was purified by passage through a trap containing activated γ-Al_2O_3 particles and zeolite 4A to remove any traces of metal carbonyls from the high-pressure gas cylinders and moisture, respectively. Zeolite HY (Zeolyst International, CBV760, Si:Al atomic ratio $\cong$ 30) was calcined in O_2 at 773 K for 4 h and evacuated for 16 h at 773 K. The support was isolated and stored in an argon-filled glovebox (MBraun, with H_2O concentrations < 0.5 ppm and O_2 concentrations < 5 ppm) until it was used. *n*-Pentane solvent (Fisher, 99%) was dried and purified by column chromatography (Grubbs apparatus, MBraun SPS) in the presence of argon.

The precursor $Rh(C_2H_4)_2(acac)$ was purchased from Strem Chemicals (99%) and used as received; the precursor $Ir(C_2H_4)_2(acac)$ was synthesized as described elsewhere.[1] To prepare the supported iridium complex, $Ir(C_2H_4)_2(C_5H_7O_2)$ and the calcined zeolite in a Schlenk flask were slurried in dried *n*-pentane that was initially at room temperature. The stirred slurry was warmed to room temperature, and after a day the solvent was removed by evacuation for a day, so that all the iridium remained on the support. The resultant solid, containing 1.0 wt% iridium; 0.54 wt% rhodium; or 0.75 wt% iridium + 0.40 wt% rhodium (Ir to Rh atomic ratio = 1) was stored in the glovebox.

IR Spectroscopy. A Bruker IFS 66v/S spectrometer with a spectral resolution of 2 cm^{-1} was used to collect transmission IR spectra of powder samples. Approximately 50 mg of solid sample in the glovebox was pressed into a thin wafer and loaded into a cell that serves as a flow reactor (In-situ Research Institute, Inc., South Bend, IN). The cell was sealed and connected to a flow system that allowed recording of spectra of the pressed wafer samples as reactant gases flowed through the cell at a specified temperature. Each spectrum is the average of 64 scans.

Catalyst Testing. Catalyst testing was carried out in a conventional laboratory once-through tubular plug-flow reactor. The catalyst (20 mg) was diluted with 10 g of particles of inert, nonporous α-Al_2O_3 loaded into the reactor in a glovebox. The feed partial pressures of C_2H_4, H_2, and helium were 100, 400, and 500 mbar, respectively, with a total flow rate of 100 mL/min and a total pressure that was atmospheric. The temperature was 298 ± 1 K, controlled with a cooling jacket filled with water.

Products were analyzed by gas chromatography by use of an HP-6890 gas chromatograph equipped with a 50 m × 0.53 mm DB-624 capillary column (J & W Scientific) and a flame-ionization detector. The effluent gas from the reactor was sampled every 12 min for analysis. Intrinsic catalytic activities (expressed as moles of ethylene converted (moles of metal × s), the turnover frequency, TOF) and selectivities were determined by operation of the reactor in the differential conversion range (conversion <5%). TOF values were calculated by assuming that all the metal atoms were accessible to the reactants. The activity of each of the catalysts decreased with time on stream as a consequence of modification of the active sites. The deactivation was likely caused by the formation of small amounts of heavier hydrocarbons, as evidenced by mass spectra of the effluent gases; these heavier hydrocarbons could poison the metal species by irreversible adsorption. To eliminate the effect of the deactivation, the activity of each catalyst was extrapolated to time on stream = 0 from the corresponding TOF *vs.* time on stream plots.

Isotopic H_2/D_2 Exchange Experiments. Measurements of mass spectra were carried out to determine the products of the reaction in a tubular plug-flow reactor identical to that mentioned above. The catalyst (20 mg) was diluted with 5 g of particles of inert, nonporous α-Al_2O_3 and was loaded into the reactor in an inert-atmosphere glovebox. The feed consisted of C_2H_4, H_2, and D_2 (the respective partial pressures were 100, 400, and 500 mbar) with the total flow rate being 100 mL/min and the total pressure being atmospheric. The temperature was 298 ± 1 K, controlled with a cooling jacket filled with water. Mass spectra of the gases introduced into the flow system and the effluents produced by reaction were measured with an online Balzers OmniStar mass spectrometer running in multi-ion monitoring mode. The HD exchange was measured at room temperature for times on stream <10 min, for which the nuclearity of the iridium and rhodium complexes initially present as single-atom complexes was maintained, as demonstrated by EXAFS spectroscopy and STEM images.

X-ray Absorption Spectroscopy. X-ray absorption spectra were recorded at X-ray beam line 4-1 at the Stanford Synchrotron Radiation Lightsource (SSRL). The storage ring electron energy and ring current were 3 GeV and 300 mA, respectively. A double-crystal Si(220) monochromator was detuned by 20–25% at the Ir L_{III} edge to minimize effects of higher harmonics in the X-ray beam.

In an N_2-filled glovebox at SSRL, the powder sample was pressed into a wafer, mounted in a cell,[2] and maintained under vacuum (10^{-5} kPa) at liquid-nitrogen temperature during the data collection. The mass of each sample (approximately 0.3 g) was chosen for optimal absorption measurements at the Ir L_{III} edge (11215 eV), giving an X-ray absorbance of approximately 2.0 calculated at an energy 50 eV greater than the absorption edge. Transmission spectra were collected by use of ion chambers mounted on each end of the sample cell. For calibration, measurement of the absorption of a platinum foil, placed after the sample, was carried out simultaneously.

EXAFS Data Analysis. The X-ray absorption edge energy was calibrated with the measured signal at the Pt L_{III} edge of the platinum foil that was scanned simultaneously with the sample. The edge was taken to be the inflection point at 11564 eV. The data were normalized by dividing the absorption intensity by the height of the absorption edge.

The EXAFS data were analyzed with the software ATHENA, which is part of the IFEFFIT[3,4] package, and with the software XDAP, developed by Vaarkamp et al.[5] Each spectrum that was analyzed was the average of two to four consecutively recorded spectra. ATHENA was used for edge calibration, deglitching, and data normalization. XDAP was used for background removal, normalization, and conversion of the data into an EXAFS (χ) file; XDAP is well designed for application of a so-called difference-file technique[6] involving analysis of individual shells, and this approach was used to determine optimized fit parameters. Each spectrum was processed by fitting a second-order polynomial to the pre-edge region and subtracting this from the entire spectrum. The functional that was minimized and the function used to model the data are reported elsewhere.[6] The background was subtracted by use of cubic spline routines. Reference backscattering phase shifts were calculated from crystallographic data with the software FEFF7[7]. $Ir(C_2H_4)_2(acac)$[1] and $Rh(C_2H_4)_2(acac)$ were used as a standard for the M–O, M–C, and M–C_{long} contributions (M = Ir or Rh); Ir-Al alloy and Rh-Al alloy[8] was used as a standard for Ir–Al and Rh–Al contributions, and iridium and rhodium metals[8] were used for Ir–Ir and Rh–Rh contributions. These contributions were selected as candidates for the EXAFS analysis because they were all considered plausible on the basis of reports of similar supported iridium complexes and clusters.[9] Iterative fitting was done in *R* (distance) space with the Fourier-transformed EXAFS (χ) data until optimum agreement was attained between the calculated k^1-, k^2-, and k^3-weighted EXAFS data and each candidate model.

The error in the data was calculated as the root mean square of the value obtained by subtraction of smoothed χ data from the background-subtracted experimental χ values. Goodness of fit values were calculated with the software XDAP with the following equation:

$$goodness\ of\ fit = \frac{\nu}{NPTS\left(\nu - N_{\text{free}}\right)} \sum_{i=1}^{NPTS} \left(\frac{\chi_{\text{exp},i} - \chi_{\text{model},i}}{\sigma_{\text{exp},i}} \right)^2$$

Here the terms χ_{model} and χ_{exp} are the model and experimental EXAFS values, respectively; σ_{exp} is the error in the experimental results; ν is the number of independent data points in the fit range; *NPTS* is the number of data points in the fit range; and N_{free} is the number of free parameters. The number of parameters used in the fitting was always less than the statistically justified number determined by the Nyquist theorem:[10] $n = (2\Delta k\Delta r/\pi) + 1$, where Δk and Δr, respectively, are the *k* (wave vector) and *r* (interatomic distance) ranges used in the fitting.

Aberration-Corrected STEM Imaging. Images were obtained with a JEOL JEM-2100F electron microscope at the University of California, Davis. The microscope was equipped with a FEG, operating at 200 kV, with a CEOS hexapole probe (STEM) aberration corrector. The images were captured with an HAADF detector with a collection semi-angle of 75–200 mrad and a probe convergence semi-angle of 17.1 mrad. The imaging dose was approximately 10^5 e^- $Å^{-2}$. Prior to imaging of each sample, the aberration corrector was aligned with a Pt/Ir on holey carbon standard sample (SPI supplies) until atomic resolution of the metal particles was achieved and the lattice spacing was confirmed of the metals in the standard sample were confirmed.

Sample Handling for Electron Microscopy. To minimize the exposure to air and moisture, powder samples in the argon-filled glovebox were loaded onto a lacey carbon film, 300-mesh copper grid (Ted-Pella). The grid was placed into an Eppendorf tube that was sealed with Parafilm®. Still in the glovebox, each Eppendorf tube was placed into a stainless-steel Swagelok tube sealed with O-rings for transfer to the microscope. There, an argon-filled glovebag (Glas-Col) was purged five times with ultra-high-purity argon (Praxair, Grade 5.0), and the TEM grid was loaded onto the TEM holder under a blanket of flowing argon in the glovebag. The TEM holder was then inserted into the nearby microscope under a flow of argon, with any exposure to air lasting less than 5 s.

Table S1 Catalytic results characterizing HY zeolite-supported rhodium, iridium or rhodium + iridium complexes for conversion of ethylene in the presence of H_2 at 298 K and 1 bar.[a]

Catalyst	Reactant(s)	TOF[c] (s^{-1})	Selectivity (%)		
			ethane	butenes	butane
Rh/zeolite	C_2H_4[a]	3.5×10^{-3}	8.1	91.9	0
Ir/zeolite		1.0×10^{-3}	6.2	93.8	0
(Rh + Ir)/zeolite		1.1×10^{-3}	7.3	92.7	0
Rh/zeolite + Ir/zeolite[d]		2.6×10^{-3}	6.5	93.5	0
Rh/zeolite	$C_2H_4 + H_2$[b]	0.39	24.3	73.9	1.8
Ir/zeolite		0.43	71.7	27.1	1.2
(Rh + Ir)/zeolite		0.30	71.4	26.3	2.3
Rh/zeolite + Ir/zeolite[d]		0.40	52.8	44.8	2.4

[a] Reactions preformed at 100 mbar of C_2H_4 and 500 mbar of helium with total flow rate of 100 mL/min. [b] Reactions preformed at 100 mbar of C_2H_4, 400 mbar of H_2 and 500 mbar of helium with total flow rate of 100 mL/min. [c] Turnover frequencies determined at time-on-stream = 0 from the corresponding TOF vs. time-on-stream curves. [d] Physical mixture of the two catalysts.

Table S2 Summary of structural parameters corresponding to the fit models characterizing EXAFS data representing HY zeolite supported catalysts incorporating both iridium and rhodium complexes (at room temperature and 1 bar).

Catalyst	Absorber – back-scatterer pair	*N*	*R* (Å)	$10^3 \times \Delta\sigma^2$ (Å^2)	ΔE_0 (eV)	*k* range (Å^{-1})	*R* range (Å)	*Error in EXAFS function*	*Good-ness of fit*
IrRh/zeolite in helium at Ir L_{III} edge	Ir–$O_{zeolite}$	1.9	2.20	10	-4.7	3.79–12.16	0.5–3.5	0.0007	8.2
	Ir–C	4.1	2.09	4.4	-4.5				
	Ir–Al	1.0	2.95	7.6	-0.38				
	Ir–M	[a]	[a]	[a]	[a]				
IrRh/zeolite after being in H_2 and C_2H_4 for 20 min at Ir L_{III} edge	Ir–$O_{zeolite}$	1.9	2.17	13	-4.7	3.83–11.45	0.5–3.5	0.0005	5.4
	Ir–C	2.1	2.10	4.8	-6.0				
	Ir–Al	1.1	2.98	6.0	-7.1				
	Ir–M	[a]	[a]	[a]	[a]				
IrRh/zeolite in helium at Rh K edge	Rh–$O_{zeolite}$	2.0	2.15	13	6.97	3.63–11.65	0.5–3.5	0.0003	6.0
	Rh–C	4.2	2.07	4.7	4.32				
	Rh–Al	1.1	3.10	11	0.72				
	Rh–M	[a]	[a]	[a]	[a]				
IrRh/zeolite after being in H_2 and C_2H_4 for 20 min at Rh K edge	Rh–$O_{zeolite}$	1.9	2.15	10	7.9	3.54–11.14	0.5–3.5	0.0002	13
	Rh–C	2.0	2.04	2.6	5.7				
	Rh–Al	1.1	3.09	12	3.8				
	Rh–M	[a]	[a]	[a]	[a]				

[a] Contribution not detectable. [b] Fit details: $0.5 < R < 3.2$ Å, $3.84 < k < 12.06$ Å^{-1}, error: 0.0006, goodness of fit: 5.7. [c] Notation: M, Ir or Rh; *N*, coordination number; *R*, distance between absorber and backscatterer atoms; $\Delta\sigma^2$, disorder term, sometimes called Debye-Waller factor; ΔE_0, inner potential correction. Error bounds (accuracies) characterizing the structural parameters obtained by EXAFS spectroscopy are estimated to be as follows: *N*, ±20%; *R*, ±0.02 Å; $\Delta\sigma^2$, ±20%; and ΔE_0, ±20%. [d] The number of statistically justified parameters was calculated according to the Nyquist theorem as follows: number of justified parameters $n = (2\Delta k\Delta R/\pi) + 2$, where Δk and ΔR are the *k*- and *R*-ranges used for the fitting, respectively.

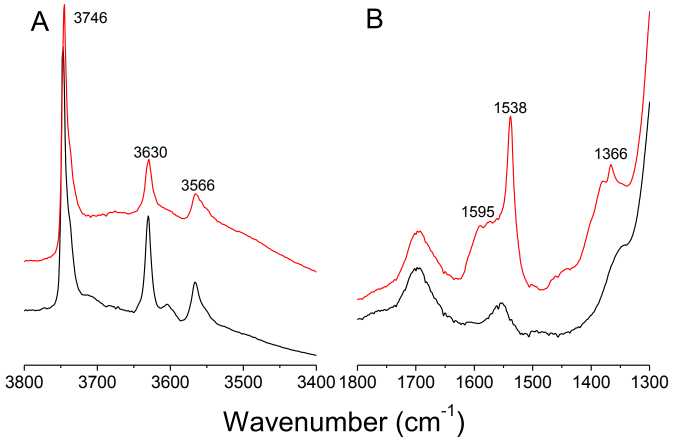

Fig. S1 IR spectra (absorbance) in the ν_{OH} (A) and 1300–1700-cm^{-1} (B) regions characterizing the following samples: HY zeolite after calcination (bottom) and sample formed by reaction of the zeolite with $Ir(C_2H_4)_2(acac)$ and $Rh(C_2H_4)_2(acac)$ after removal of the *n*-pentane solvent (top).

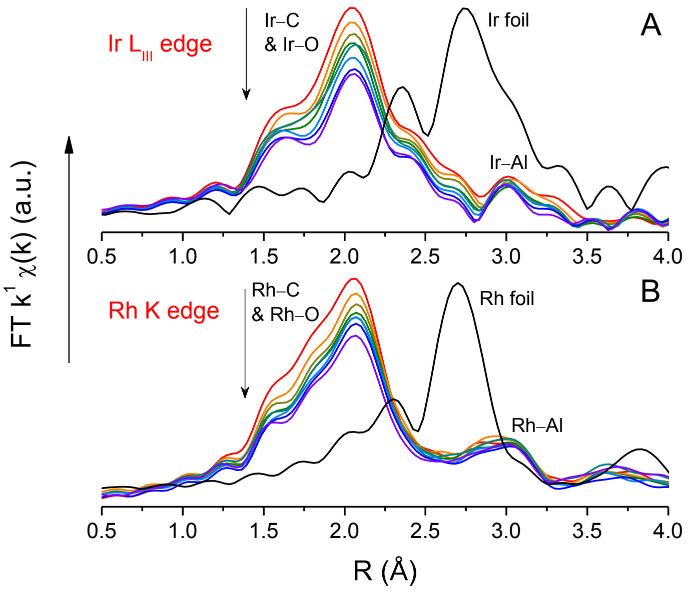

Fig. S2 Transient Fourier-transformed EXAFS spectra at Ir L_{III} and Rh K edges characterizing sample initially incorporating $Ir(C_2H_4)_2$ and $Ir(C_2H_4)_2$ on the same HY zeolite in flowing helium (topmost spectra) and in flowing C_2H_4 and H_2 (1 : 4 molar ratio) over a period of 20 min (from top to bottom). EXAFS spectra of iridium and rhodium foils are also plotted for comparison.

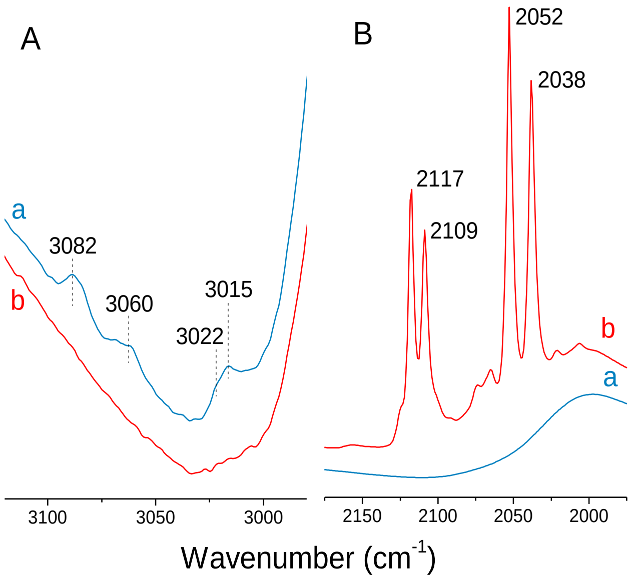

Fig. S3 IR spectra (absorbance) in the ν_{CH} (A) and ν_{CO} (B) regions characterizing the sample formed by adsorption Ir(C_2H_4)$_2$(acac) and Rh(C_2H_4)$_2$(acac) on HY zeolite as it was treated in flowing gases at 298 K and 1 bar, as follows: (a) helium and (b) a pulse (20 mL) of CO in helium.

Interpretation and discussion of Figures S1-S3:

Fig. S1 shows IR spectra in the ν_{OH} and 1300–1700 regions characterizing HY zeolite before and after reaction with Ir(C_2H_4)$_2$(acac) and Rh(C_2H_4)$_2$(acac) precursors. In the ν_{OH} region, the bands at 3566 and 3630 cm^{-1} are assigned to the acidic Al–OH groups of the zeolite and the band at 3746 cm^{-1} is assigned to terminal Si–OH groups.[11,12] The observation that the 3566 and 3630 cm^{-1} bands decreased in intensity after the reaction with the precursors while the intensity of the 3746 cm^{-1} bands stayed unchanged suggest the precursors preferentially reacted with the acidic Al–OH sites where the acac ligands are removed by reaction with the protons. This inference is bolstered by the IR spectra in the 1300–1700 region showing appearance of bands at 1355, 1536, and 1585 cm^{-1}, assigned to δ_{CH}, ν_{C-C-Cs}, and ν_{COring} and resembling those characterizing Hacac adsorbed on the zeolite.[13,14] Furthermore, the IR spectra suggest the ethylene ligands from the precursors remain bonded to the metals after synthesis. This is evidenced by the IR bands in the ν_{CH} region at 3015, 3022, 3060 and 3082 cm^{-1} characterizing the initially prepared IrRh/zeolite sample (Fig. S3); the 3022 and 3082 cm^{-1} bands and the 3015 and 3060 cm^{-1} bands are assigned to ν_{CH} of ethylene π-bonded to iridium and rhodium, respectively,[15,16] precisely matching those characterizing Ir/zeolite and Rh/zeolite.[17,18]

EXAFS data characterizing the initially prepared sample incorporating supported iridium and rhodium species were measured at the Ir L_{III} and Rh K edges. The quantitative results from analysis of the spectra at both Ir and Rh edges (Table S1) include M–C, M–O and M–Al contributions with coordination numbers (CN) of approximately 4, 2 and 1, respectively. These results essentially matches with IR results, demonstrating the supported iridium and rhodium complexes are isostructural, with each metal atom bonded approximately to two ethylene ligands and two support oxygen atoms at the Al centers of the zeolite. Moreover, both qualitative observations based on the Fourier-transformed EXAFS spectra (Fig. S2) and quantitative analysis of the EXAFS data show no evidence of Ir–Ir or Rh–Rh contributions at 2.6–2.7 Å (i.e. typical metal–metal bonding distances of Group-9 metals[19]), suggesting mononuclear rhodium and iridium complexes are the only metal species present in the sample.

When the initially prepared IrRh/zeolite catalyst is brought into contact with a pulse (20 mL) of CO in flowing helium at 298 K and 1 bar, displacement of the C_2H_4 ligands by CO ligands took place rapidly, as indicated in the IR spectra (Fig. S3) by the disappearance of the ν_{CH} bands at 3015, 3022, 3060 and 3082 cm^{-1} and concomitant appearance of four sharp bands in the ν_{CO} region at 2038, 2052, 2109 and 2117 cm^{-1}. The new bands at 2018 and 2109 cm^{-1} are assigned to iridium *gem*-dicarbonyls;[20,21] and the new bands at 2052 and 2117 cm^{-1} are assigned to rhodium *gem*-dicarbonyls.[22,23,24] Moreover, the new ν_{CO} bands are quite narrow, with full width at half maximum (fwhm) being less than 10 cm^{-1}, indicating those supported iridium and rhodium complexes have high degrees of uniformity.[25]

In summary, the IR and EXAFS spectra show that the iridium and rhodium species in IrRh/zeolite catalyst consist of isolated isostructural $Ir(C_2H_4)_2$ and $Rh(C_2H_4)_2$ complexes which were bonded, on average, to two support oxygen atoms at the Al centers of the zeolite, with no evidence of metal clusters. Moreover, the structures and metal–support interfaces of the iridium and rhodium complexes in the IrRh/zeolite catalysts were indistinguishable from those in the Ir/zeolite and Rh/zeolite catalysts.

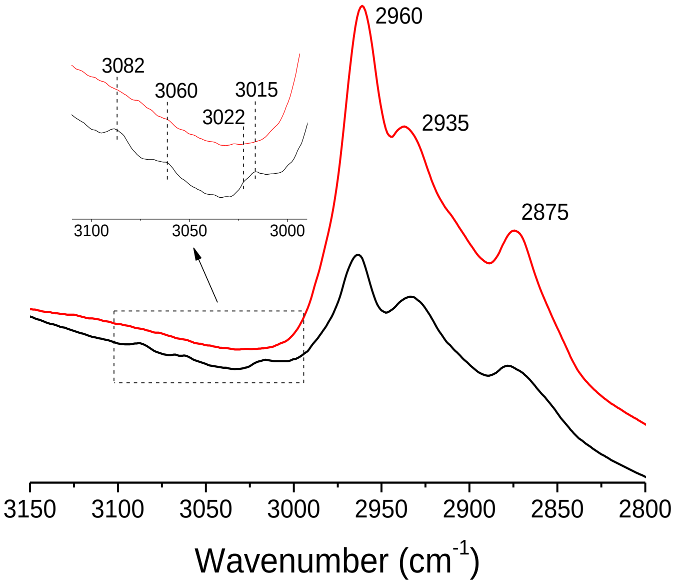

Fig. S4 IR spectra (absorbance) in the ν_{CH} region characterizing the sample formed by adsorption $Ir(C_2H_4)_2(acac)$ and $Rh(C_2H_4)_2(acac)$ on HY zeolite as it was treated in flowing C_2H_4 and H_2 at 298 K and 1 bar for 0 (bottom) and 10 min (top).

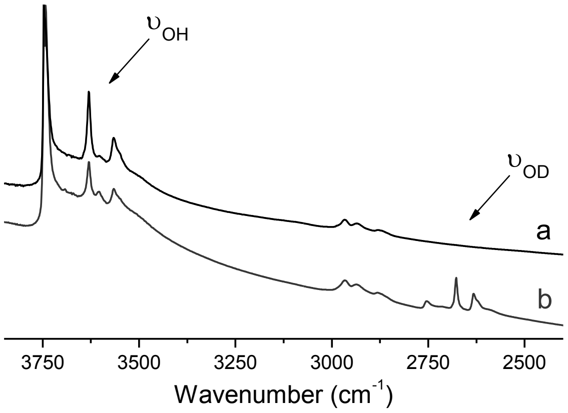

Fig. S5 IR spectra (absorbance) in the ν_{OH} and ν_{OD} regions characterizing Ir/zeolite treated in flowing (a) helium and (b) $H_2 + D_2$ (equal molar) at 298 K and 1 bar.

Characterization of the (Rh + Ir)/zeolite Catalyst during Ethylene Hydrogenation/Dimerization Catalysis:

The possibility that the predominant rhodium and iridium species in the bimetallic catalyst were different from those in the monometallic catalysts is ruled out by the spectra and images. EXAFS spectra at the Rh K and Ir L_{III} edges characterizing the bimetallic catalyst (Figure S2) show a rapid decrease in magnitude of the contributions centred at ~2.1 Å (assigned to the combination of M–$O_{support}$ and M–C contributions) once the bimetallic catalyst was brought into contact with a flowing mixture of ethylene + H_2, whereas no such decrease was observed for the contribution at ~3.0 Å (assigned to the M–Al contribution). These data indicate that changes occurred in the ligand environments of both metals during catalysis and that both metals remained stably bonded to the support. The EXAFS structural parameters of the catalysts after 20 min of operation in flowing ethylene + H_2 (Table S1) demonstrate a decrease in the coordination numbers (CN) characterizing the Rh–C and Ir–C contributions, each from approximately 2 to approximately 1. The change in the Ir–C coordination of the bimetallic catalyst was confirmed by the IR spectra characterizing RhIr/zeolite treated in flowing ethylene + H_2 (Figure S4), showing the disappearance of the 3015-, 3022-, 3060-, and 3082-cm^{-1} bands assigned to ν_{CH} vibrations of ethylene ligands initially π-bonded to the iridium and rhodium,[17,18] and the concomitant growth of bands at 2960, 2935 and 2875 cm^{-1} assigned to the ν_{CH} vibrations of alkyl species σ-bonded to the metals.[26]

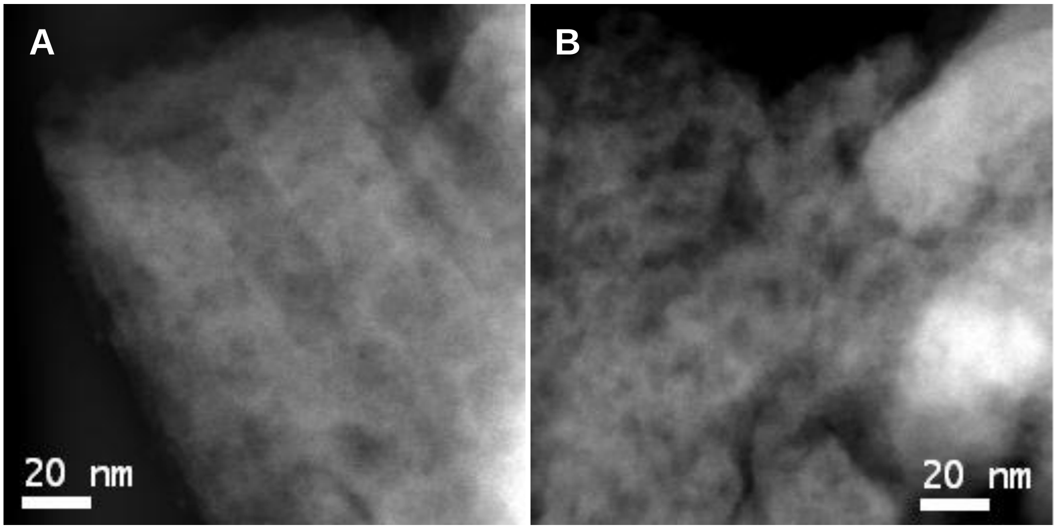

Figure S6. Aberration-corrected HAADF-STEM images of bimetallic catalyst: (A) sample as initially synthesized from $Rh(C_2H_4)_2(acac)$ and $Ir(C_2H_4)_2(acac)$. (B) Sample after treatment in C_2H_4 and H_2 for 20 min. The images are at lower magnifications than those shown in Figure 1 in the main text, confirming the absence of metal clusters in both samples.

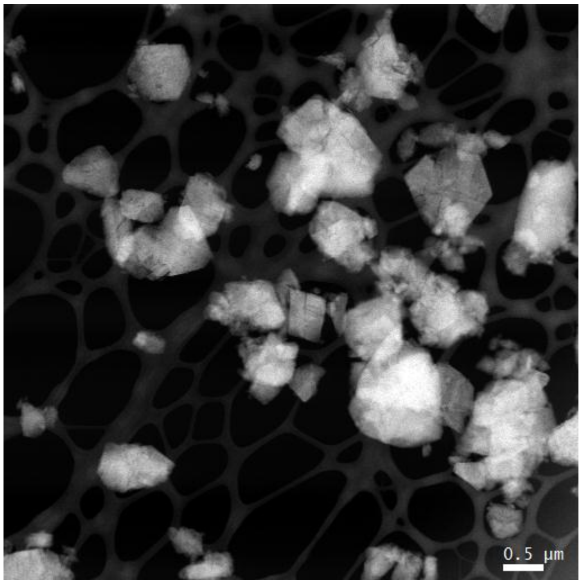

Fig. S7 STEM images of HY zeolite powder showing the radius of the average diameters of the zeolite crystals are approximately 800 nm.

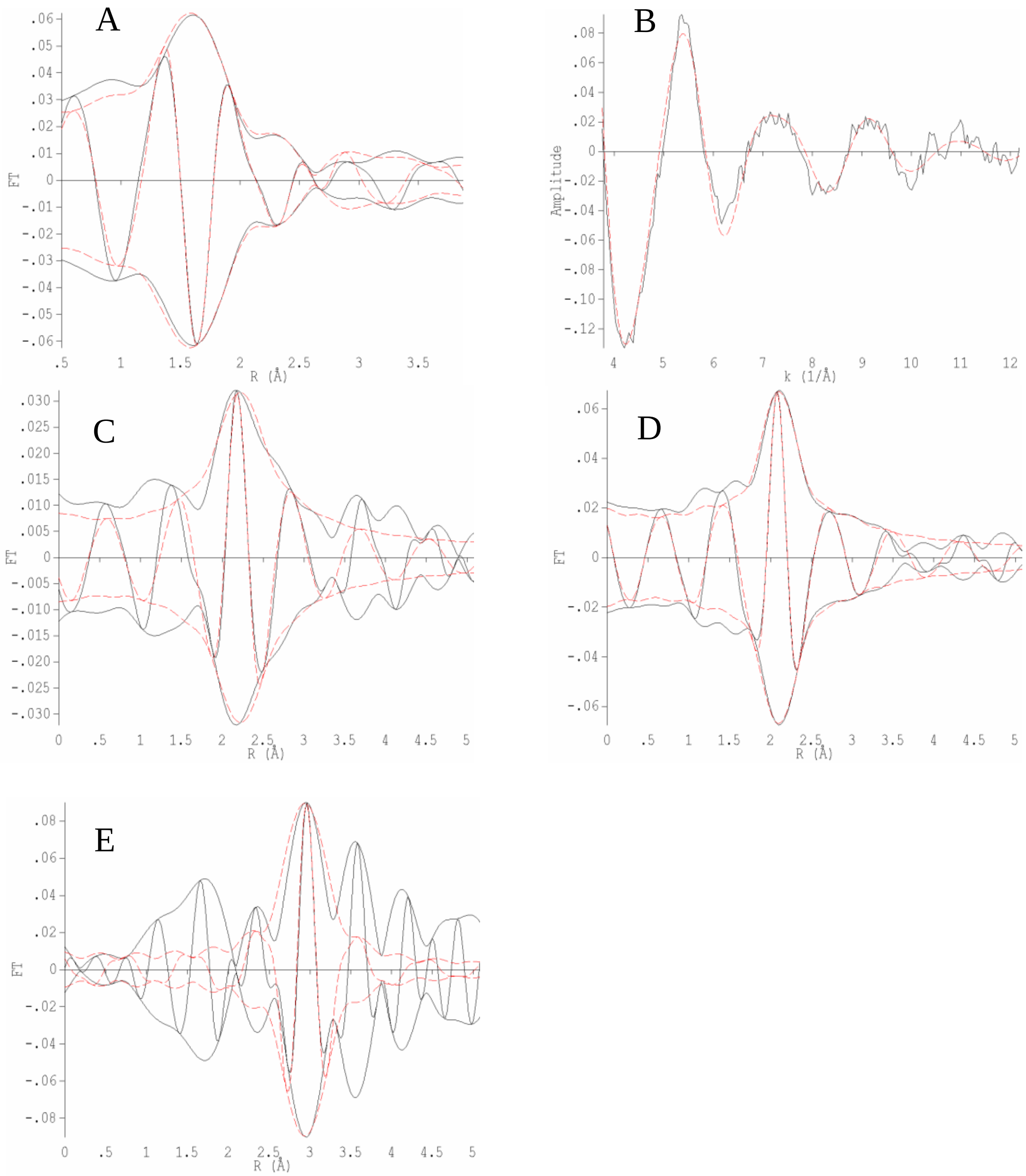

Fig. S8 EXAFS data characterizing initially prepared HY zeolite-supported iridium complex formed by adsorption of $Ir(C_2H_4)_2(acac)$ on the zeolite: (A) k^1-weighted EXAFS function, $k^1(\chi)$ (solid line) and sum of the calculated contributions (dashed line); (B) k^1-weighted imaginary part and magnitude of the Fourier transform of the data (solid line) and sum of the calculated contributions (dashed line); (C) k^1-weighted, phase-corrected, imaginary part and magnitude of the Fourier transform of the data (solid line) and calculated contributions (dashed line) of Ir–$O_{support}$ shell; (D) k^1-weighted, phase-corrected, imaginary part and magnitude of the Fourier transform of the data (solid line) and calculated contributions (dashed line) of Ir–C shell; (E) k^2-weighted, phase-corrected, imaginary part and magnitude of the Fourier transform of the data (solid line) and calculated contributions (dashed line) of Ir–Al shell.

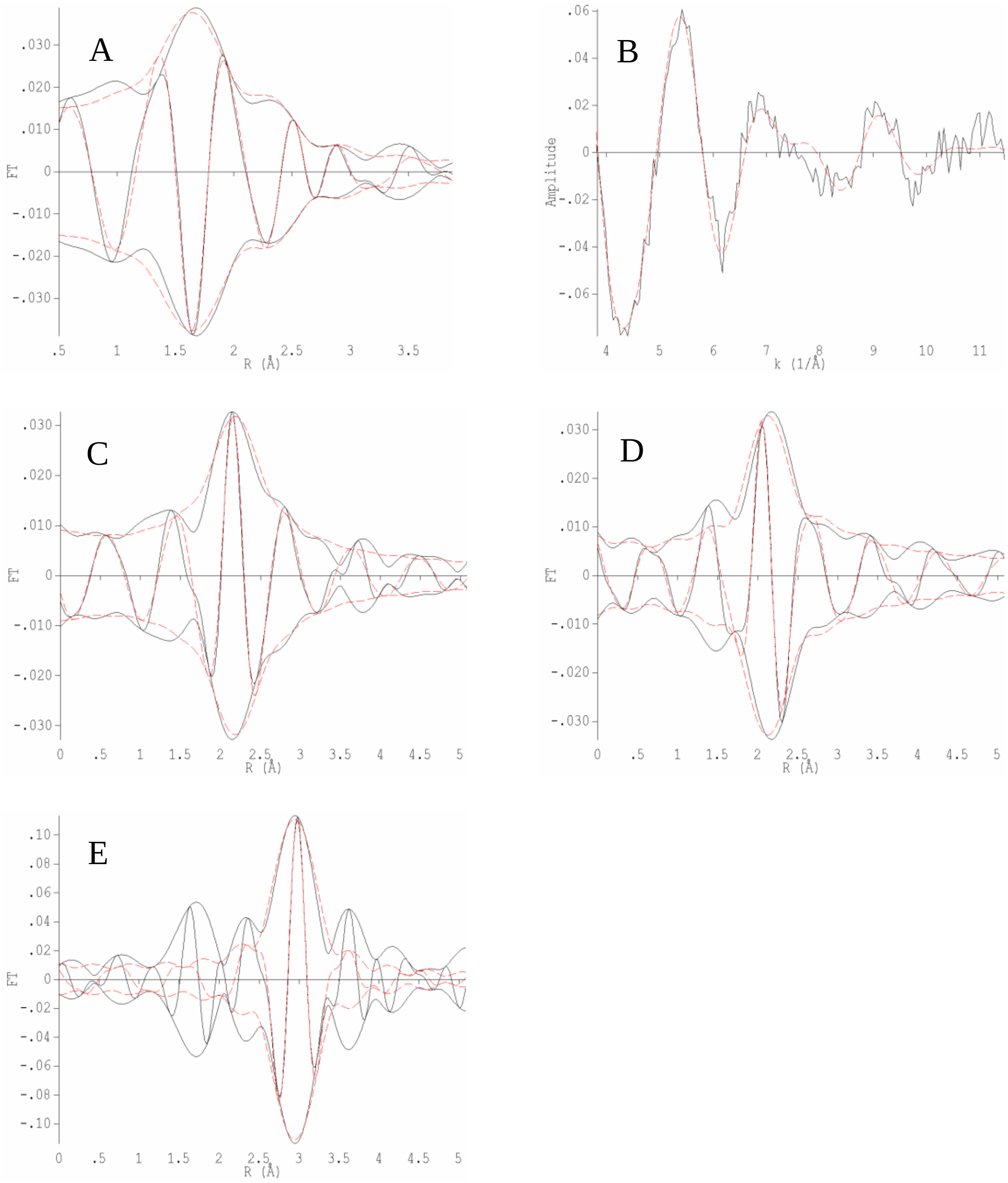

Fig. S9 EXAFS data characterizing HY zeolite-supported iridium complex formed by adsorption of $Ir(C_2H_4)_2(acac)$ on the zeolite after treatment in C_2H_4 + H_2 at 298 K for 20 min: (A) k^1-weighted EXAFS function, $k^1(\chi)$ (solid line) and sum of the calculated contributions (dashed line); (B) k^1-weighted imaginary part and magnitude of the Fourier transform of the data (solid line) and sum of the calculated contributions (dashed line); (C) k^1-weighted, phase-corrected, imaginary part and magnitude of the Fourier transform of the data (solid line) and calculated contributions (dashed line) of Ir–$O_{support}$ shell; (D) k^1-weighted, phase-corrected, imaginary part and magnitude of the Fourier transform of the data (solid line) and calculated contributions (dashed line) of Ir–C shell; (E) k^2-weighted, phase-corrected, imaginary part and magnitude of the Fourier transform of the data (solid line) and calculated contributions (dashed line) of Ir–Al shell.

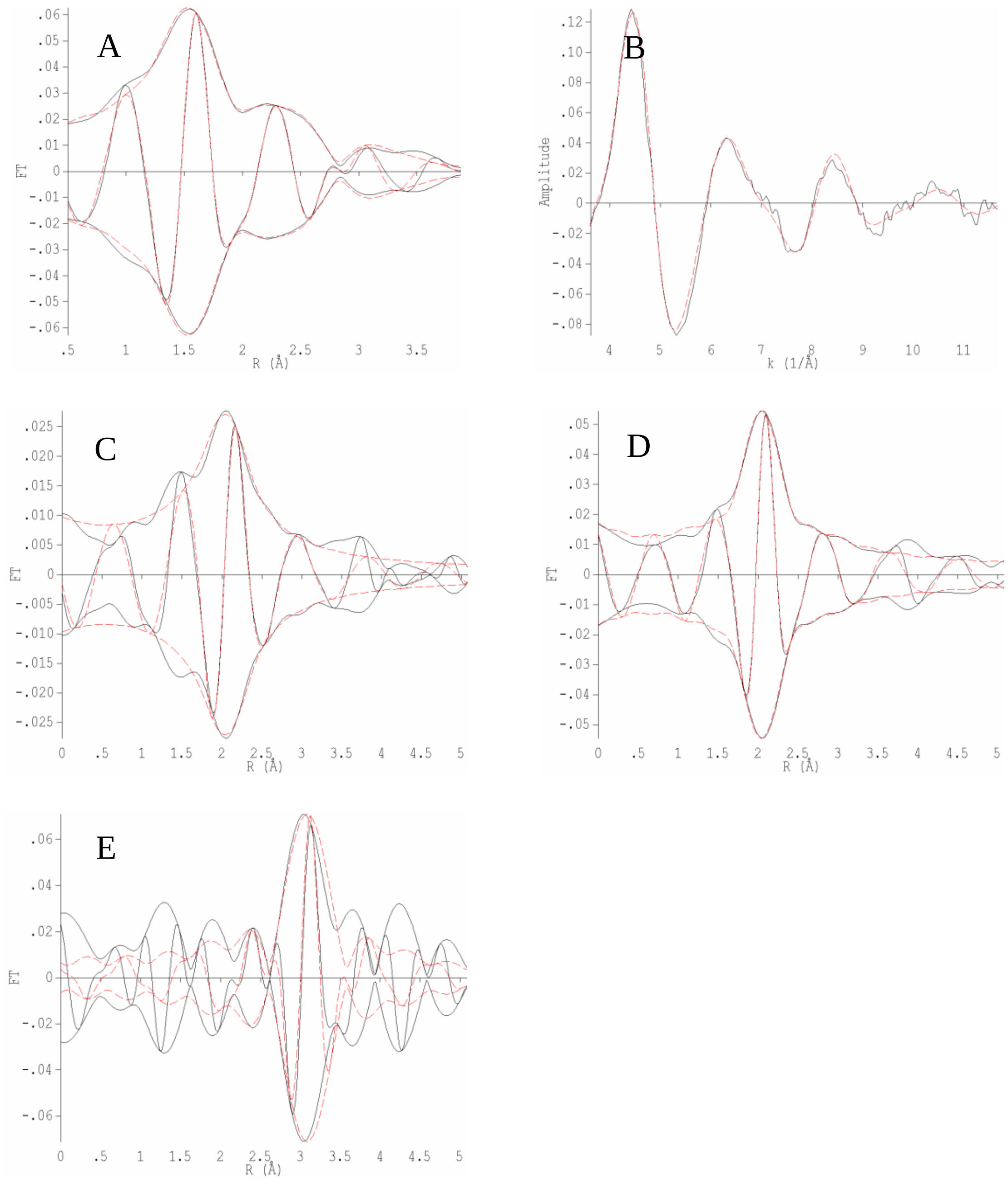

Fig. S10 EXAFS data characterizing initially prepared HY zeolite-supported rhodium complex formed by adsorption of $Rh(C_2H_4)_2(acac)$ on the zeolite: (A) k^1-weighted EXAFS function, $k^1(\chi)$ (solid line) and sum of the calculated contributions (dashed line); (B) k^1-weighted imaginary part and magnitude of the Fourier transform of the data (solid line) and sum of the calculated contributions (dashed line); (C) k^1-weighted, phase-corrected, imaginary part and magnitude of the Fourier transform of the data (solid line) and calculated contributions (dashed line) of Rh–$O_{support}$ shell; (D) k^1-weighted, phase-corrected, imaginary part and magnitude of the Fourier transform of the data (solid line) and calculated contributions (dashed line) of Rh–C shell; (E) k^2-weighted, phase-corrected, imaginary part and magnitude of the Fourier transform of the data (solid line) and calculated contributions (dashed line) of Rh–Al shell.

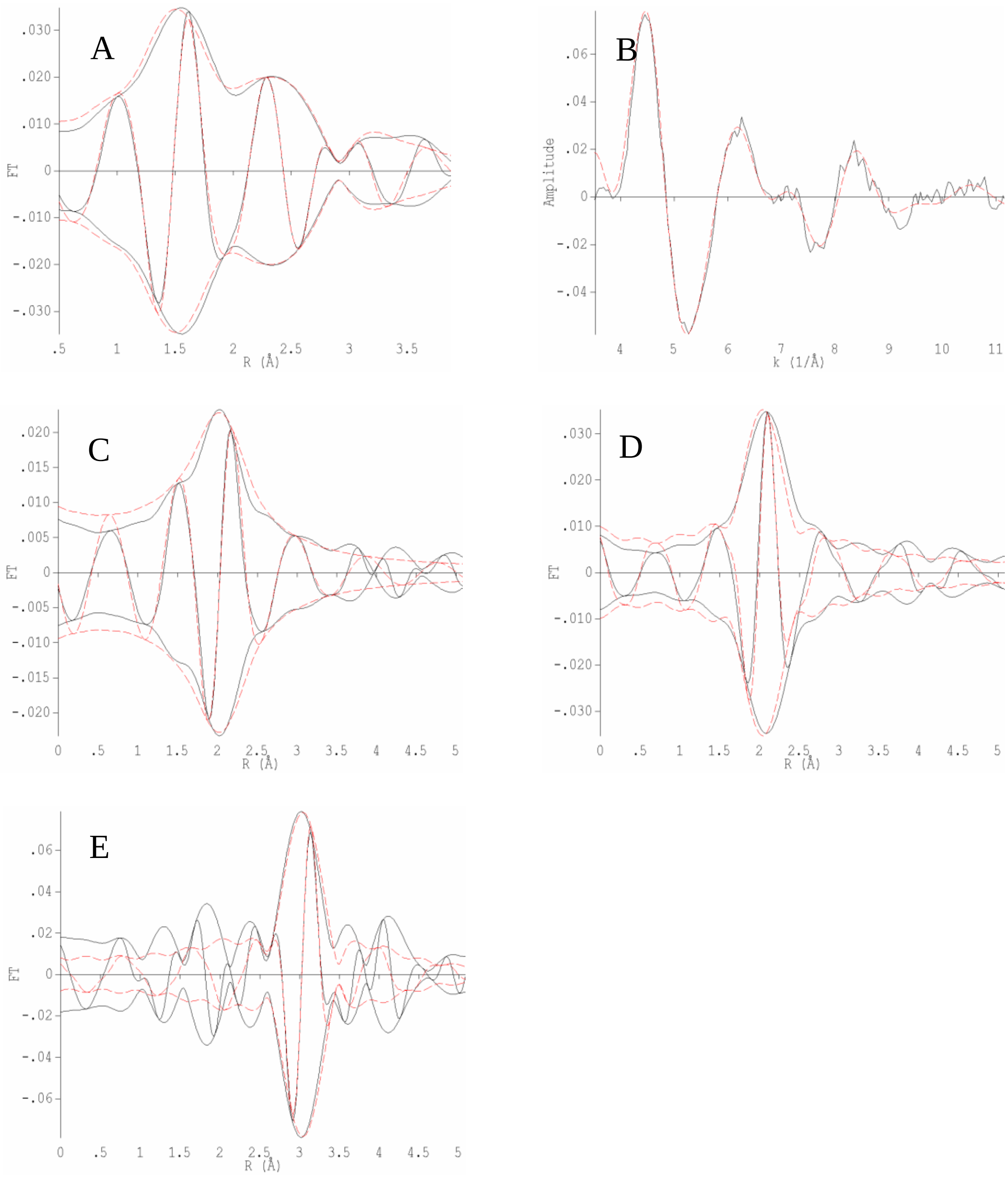

Fig. S11 EXAFS data characterizing HY zeolite-supported iridium complex formed by adsorption of $Rh(C_2H_4)_2(acac)$ on the zeolite after treatment in C_2H_4 + H_2 at 298 K for 20 min: (A) k^1-weighted EXAFS function, $k^1(\chi)$ (solid line) and sum of the calculated contributions (dashed line); (B) k^1-weighted imaginary part and magnitude of the Fourier transform of the data (solid line) and sum of the calculated contributions (dashed line); (C) k^1-weighted, phase-corrected, imaginary part and magnitude of the Fourier transform of the data (solid line) and calculated contributions (dashed line) of Rh–$O_{support}$ shell; (D) k^1-weighted, phase-corrected, imaginary part and magnitude of the Fourier transform of the data (solid line) and calculated contributions (dashed line) of Rh–C shell; (E) k^2-weighted, phase-corrected, imaginary part and magnitude of the Fourier transform of the data (solid line) and calculated contributions (dashed line) of Rh–Al shell.

References

(1) V. A. Bhirud, A. Uzun, P. W. Kletnieks, R. Craciun, J. F. Haw, D. A. Dixon, M. M. Olmstead, B. C. Gates, *J. Organomet. Chem.* **2007**, *692*, 2107–2113.

(2) R. E. Jentoft, S. E. Deutsch, B. C. Gates, *Rev. Sci. Instrum.* **1996**, *67*, 2111.

(3) M. Newville, B. Ravel, D. Haskel, J. J. Rehr, E. A. Stern, Y. Yacoby, *Physica B* **1995**, *208/209*, 154.

(4) M. Newville, *J. Synchrotron Rad.* **2001**, *8*, 96–100.

(5) M. Vaarkamp, J. C. Linders, D. C. Koningsberger, *Physica B* **1995**, *209*, 159.

(6) D. C. Koningsberger, B. L. Mojet, G. E. van Dorssen, D. E. Ramaker, *Top. Catal.* **2000**, *10*, 143.

(7) S. E. Zabinsky, J. J. Rehr, A. Ankudinov, R. C. Albers, M. J. Eller, *Phys. Rev. B.* **1995**, *52*, 2995.

(8) W. B. Pearson, L. D. Calvert, P. Villars, Pearson's Handbook of Crystallographic Data for Intermetallic Phases; American Society for Metals: Metals Park, OH, **1985**.

(9) J. C. Fierro-Gonzalez, S. Kuba, Y. Hao, B. C. Gates, *J. Phys. Chem. B* **2006**, *110*, 13326.

(10) F. W. Lytle, D. E. Sayers, E. A. A. Stern, *Physica B* **1989**, *158*, 701.

(11) R. B. Borade, A. Clearfield, *J. Phys. Chem* **1992**, 96, 6729.

(12) A. Zecchina, F. Geobaldo, G. Spoto, S. Bordiga, G. Ricchiardi, R. Buzzoni, G. Petrini, *J. Phys. Chem.* **1996**, *100*, 16584.

(13) P. Van Der Voort, M. Mathieu, E. F. Vansant, S. N. R. Rao, M. G. White, *J. Porous Mater.* **1998**, *5*, 305.

(14) P. Van Der Voort, R. van Welzenis, M. de Ridder, H. H. Brongersma, M. Baltes, M. Mathieu, P. C. van de Ven, E. F. Vansant, *Langmuir* **2002**, *18*, 4420.

(15) A. M. Argo, J. F. Odzak, F. S. Lai, B. C. Gates, *Nature* **2002**, *415*, 623.

(16) B. E. Bent, C. M. Mate, C.-T. Kao, A. J. Slavin, G. A. Somorjai, *J. Phys. Chem.* **1988**, *92*, 4720.

(17) A. J. Liang, V. A. Bhirud, J. O. Ehresmann, P. W. Kletnieks, J. F. Haw, B. C. Gates, *J. Phys. Chem. B* **2005**, *109*, 24236.

(18) A. Uzun, V. A. Bhirud, P. W. Kletnieks, J. F. Haw, B. C. Gates, *J. Phys. Chem. C* **2007**, *111*, 15064.

(19) J. C. Fierro-Gonzalez, S. Kuba, Y. Hao, B. C. Gates, *J. Phys. Chem. B* **2006**, *110*, 13326.

(20) F. Solymosi, E. Novak, A. Molnar, *J. Phys. Chem.* **1990**, *94*, 7250.

(21) M. Mihaylov, E. Ivanova, F. Thibault-Starzyk, M. Daturi, L. Dimitrov, K. I. Hadjiivanov, *J. Phys. Chem. B* **2006**, *110*, 10383.

(22) H. Miessner, I. Burkhardt, D. Gutschick, A. Zecchina, C. Morterra, G. Spoto, *J. Chem. Soc., Faraday Trans.* **1989**, *85*, 2113.

(23) J. F. Goellner, B. C. Gates, G. N. Vayssilov, N. Rösch, *J. Am. Chem. Soc.* **2000**, *122*, 8056.

(24) E. Ivanova, M. Mihaylov, H. A. Aleksandrov, M. Daturi, F. Thibault-Starzyk, G. N. Vayssilov, N. Rösch, K. I. Hadjiivanov *J. Phys. Chem. B* **2007**, *111*, 10412.

(25) K. I. Hadjiivanov, G. N. Vayssilov, *Adv. Catal.* **2002**, *47*, 308.

(26) H. Hoffmann, P. R. Griffiths, F. Zaera, *Surf. Sci.* **1992**, *262*, 141.